

# Highly Accelerated Multishot EPI through Synergistic Combination of Machine Learning and Joint Reconstruction

Berkin Bilgic<sup>1,2,3</sup>, Itthi Chatnuntawech<sup>4</sup>, Mary Kate Manhard<sup>1,2</sup>, Qiyuan Tian<sup>1,2</sup>, Congyu Liao<sup>1,5</sup>, Stephen F. Cauley<sup>1,2</sup>, Susie Y. Huang<sup>1,2,3</sup>, Jonathan R. Polimeni<sup>1,2,3</sup>, Lawrence L. Wald<sup>1,2,3</sup>, Kawin Setsompop<sup>1,2,3</sup>

1 Athinoula A. Martinos Center for Biomedical Imaging, Charlestown, MA, USA

2 Department of Radiology, Harvard Medical School, Boston, MA, USA

3 Harvard-MIT Health Sciences and Technology, MIT, Cambridge, MA, USA

4 National Nanotechnology Center, National Science and Technology Development Agency, Pathum Thani, Thailand

5 Center for Brain Imaging Science and Technology, Key Laboratory for Biomedical Engineering of Ministry of Education, College of Biomedical Engineering & Instrument Science, Zhejiang University, Hangzhou, Zhejiang, China

## Corresponding author:

Itthi Chatnuntawech

[itthi.cha@nanotec.or.th](mailto:itthi.cha@nanotec.or.th)

**Body word count:** ~5000

## Keywords:

Multishot EPI, parallel imaging, machine learning, deep learning, convolutional neural network, joint reconstruction

## ABSTRACT

**Purpose:** To introduce a combined machine learning (ML) and physics-based image reconstruction framework that enables navigator-free, highly accelerated multishot echo planar imaging (msEPI), and demonstrate its application in high-resolution structural imaging.

**Methods:** Singleshot EPI is an efficient encoding technique, but does not lend itself well to high-resolution imaging due to severe distortion artifacts and blurring. While msEPI can mitigate these artifacts, high-quality msEPI has been elusive because of phase mismatch arising from shot-to-shot physiological variations which disrupt the combination of the multiple-shot data into a single image. We employ Deep Learning to obtain an interim magnitude-valued image with minimal artifacts, which permits estimation of image phase variations due to shot-to-shot physiological changes. These variations are then included in a Joint Virtual Coil Sensitivity Encoding (JVC-SENSE) reconstruction to utilize data from all shots and improve upon the ML solution.

**Results:** Our combined ML + physics approach enabled R=8-fold acceleration from 2 EPI-shots while providing 1.8-fold error reduction compared to the MUSSELS, a state-of-the-art reconstruction technique, which is also used as an input to our ML network. Using 3 shots allowed us to push the acceleration to R=10-fold, where we obtained a 1.7-fold error reduction over MUSSELS.

**Conclusion:** Combination of ML and JVC-SENSE enabled navigator-free msEPI at higher accelerations than previously possible while using fewer shots, with reduced vulnerability to poor generalizability and poor acceptance of end-to-end ML approaches.

## INTRODUCTION

Slow image encoding has constrained clinical MRI scans to use 2-dimensional encoding and thick slices, often with slice gaps, so that whole-brain exams can be completed within acceptable time frames. In addition to the information loss, such inefficient acquisition poses a barrier to MRI evaluation of hospitalized patients who are critically ill and can neither hold still nor tolerate long scans. Low patient throughput due to inefficient imaging also increases the time from symptom onset to diagnosis, thereby delaying treatment.

To overcome the slow image encoding barrier, recent screening protocols have moved to singleshot Echo Planar Imaging (ssEPI) to provide multi-contrast information (1,2). Unfortunately, the reduced geometric fidelity of these protocols may confound/obscure localization of salient imaging findings. The problem arises from severe distortion and blurring artifacts in ssEPI at high in-plane resolutions, where a large area of k-space has to be covered within a single readout in the presence of B0 inhomogeneity and T2\* signal decay. These effects are only partially mitigated at relatively high (R=3) in-plane acceleration.

While multishot EPI (msEPI) can mitigate blurring and distortion, high-quality msEPI has been elusive because combining the multiple-shot data into a single image is prohibitively difficult, especially at high in-plane acceleration. Image phase mismatches between the shots caused by physiological variations (respiration, cardiac pulsation) leads to severe ghosting artifacts. To date, the application of msEPI has been restricted to diffusion imaging, where two types of solutions have been proposed to combine the shots: (i) navigator-based approaches that require additional data acquisition to capture shot-to-shot phase variations (3–7), and (ii) navigator-free techniques that estimate these variations from the data itself (8–11). In (ii), multiplexed sensitivity encoding (MUSE) (9) and its extensions (8,10), rely on parallel imaging to reconstruct an intermediate image for each shot independently to estimate the physiological variations before jointly reconstructing all multishot data together. This limits the achievable distortion and blurring reduction to 4 to 6-fold, since parallel imaging with modern RF receive coil arrays breaks down beyond such acceleration in the phase-encoding direction. MUSSELS, on the other hand, does not explicitly estimate the phase of each shot image, but employs sensitivity encoding and similarities across multishot data in the form of structured low-rank matrix completion (11,12). This has allowed MUSSELS to demonstrate R=8-fold acceleration from 4-shots, reducing the number of shots to below the acceleration factor for the first time, to improve acquisition efficiency while reducing distortion and blurring artifacts. It is important to note another class of navigator-free multishot diffusion imaging techniques, which utilize non-Cartesian trajectories that allow for estimation of low-resolution image phase information from the densely sampled portion of each shot (13,14). Such self-navigation property comes at the cost of blurring/distortion compromise in the resulting images.

In this contribution, we introduce a new reconstruction framework that utilizes a synergistic combination of machine learning (ML) and physics (or forward-model) based reconstruction, and demonstrate its application for rapid structural msEPI with high geometric fidelity. We term our combined

ML + physics approach Network Estimated Artifacts for Tempered Reconstruction (NEATR). We start from MUSSELS reconstruction of a highly accelerated msEPI using a smaller number of acquisition shots, and pass the intermediate magnitude-valued solution through our deep neural network to mitigate the reconstruction artifacts from MUSSELS. Using this interim magnitude image with minimal artifacts allows us to solve for the image phase of each shot using phase-regularized parallel imaging (15). Given the phase of each shot, we then perform a Joint Virtual Coil Sensitivity Encoding (JVC-SENSE) reconstruction where we utilize the k-space data from all shots as well as virtual coil concept (16–18) to solve for the combined magnitude image.

We demonstrate the application of NEATR in spin-and-gradient-echo (SAGE (19)) msEPI acquisition at R=8-fold acceleration using 2-shots, and push the acceleration to R=10 using 3-shots. Compared to our implementation of state-of-the-art MUSSELS reconstruction, which is also used as an input to our network, we demonstrate up to 1.8-fold improvement in root-mean-squared error (RMSE) with high-quality images. This is made possible by the Deep Learning step that enables phase estimations at such high acceleration factors. But importantly, the final use of a rigorous physics-based forward-model reconstruction limits the role of ML in the final reconstruction. Thus, NEATR allows us to tap into the potential of convolutional neural networks (CNN) to solve for important nuisance modulations and unknowns in the forward model without treating the reconstruction as an end-to-end process. The result is a better harnessed sensitivity encoding with full utilization of the scanner hardware. Our strategy paves the way to reaping the benefits of ML while constraining potential damage from utilizing it on data beyond its training experience, and without being exposed to the vulnerabilities of not knowing exactly what the reconstruction is doing. We think that our approach of using ML to estimate nuisance parameters that are hard to determine could allow physics-based reconstructions to work well in other applications, such as retrospective motion-correction without navigation or additional hardware.

We provide Matlab source code and data to reproduce our results, with a function call to Python to perform the ML reconstruction, here: <https://bit.ly/2OLSG9P>

## METHODS

### Reconstruction Overview

The NEATR flowchart is presented in **Fig. 1**. We begin by performing a MUSSELS reconstruction (11) on the highly-accelerated ( $R=8$ ) msEPI data to obtain an initial image estimate with mitigated artifacts from the nuisance phase between shots. The image is further improved using U-Net processing (20) which estimates a refined magnitude image with minimal artifacts. Starting from this magnitude, we estimate the phase image corresponding to each shot using phase-regularized parallel imaging (21). Given the estimated shot-to-shot phase variations, we then perform a physics-based joint reconstruction (JVC-SENSE) to arrive at the final solution. JVC-SENSE uses k-space data from all shots and their conjugate symmetric counterparts to solve for a common magnitude image. We detail the individual steps next.

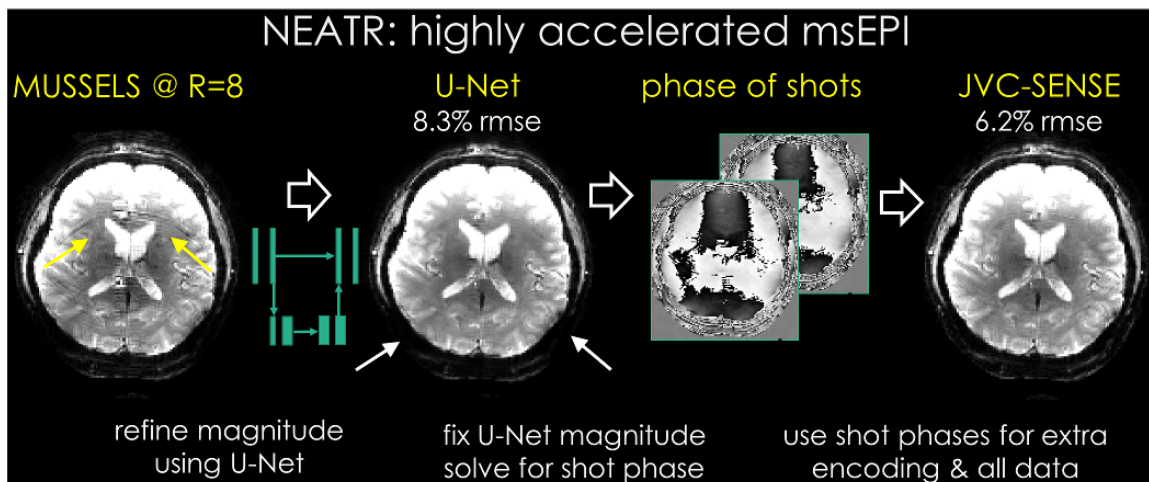


*Fig 1.* NEATR is a combined machine learning and physics-based reconstruction technique for highly-accelerated msEPI acquisition. We use the state-of-the-art MUSSELS algorithm to provide an initial solution, which suffers from aliasing artifacts (yellow arrows, left) at high acceleration ( $R=8$  with 2-shots). Starting from this, residual learning with U-Net architecture provides a magnitude image with minimal artifacts (white arrows point to underestimation, more visible in the difference images in Fig3). Given this magnitude solution, phase cycling algorithm is used for estimating shot-phases, which are then utilized as sensitivity variations in a final joint virtual coil (JVC) SENSE reconstruction.

### MUSSELS Formalism

The first step of NEATR is based on a MUSSELS reconstruction, where the input is the acquired multi-shot k-space data, and the output is a magnitude estimate which is further refined in the later steps. MUSSELS entails the solution of the following optimization problem:

$$\min_{\mathbf{x}} \sum_{t=1}^{N_s} \|F_t C \mathbf{x}_t - \mathbf{d}_t\|_2^2 + \lambda \|\mathcal{H}(\mathbf{x})\|_* \quad \text{Eq1}$$

where  $F_t$  represents the undersampled discrete Fourier transform (DFT) corresponding to shot  $t$ ,  $C$  are the coil sensitivities,  $\mathbf{x}_t$  is the unknown complex-valued image in shot  $t$  with size  $N_1 \times N_2$ , and  $\mathbf{d}_t$  are the acquired k-space data in this shot. The term  $\|F_t C \mathbf{x}_t - \mathbf{d}_t\|_2^2$  thus represents our data consistency through

sensitivity encoding (22). The operator  $\mathcal{H}(\cdot)$  first applies the DFT, and then extracts  $r \times r \times N_s$  patches in k-space to generate a data matrix  $\mathcal{H}(\mathbf{x})$  with block-wise Hankel structure (11,23–25). This operator acts on a 3-dimensional data structure  $\mathbf{x}$  of size  $N_1 \times N_2 \times N_s$ , which is formed by concatenating the images  $x_t$  from all  $N_s$  shots together. The nuclear norm constraint  $\|\mathcal{H}(\mathbf{x})\|_*$  thus enforces a low-rank prior on the block-Hankel representation of the multishot data in k-space. This prior is similar to the SAKE formulation (25), albeit with two differences: the coil axis is now replaced by the shot dimension, and sensitivity encoding is explicitly exploited. As such, we follow the SAKE approach and pursue a simple, POCS-SENSE like algorithm (26) to solve Eq1 as detailed in the Appendix. After convergence, we compute the complex average across the individual shot images and take the absolute value to arrive at the magnitude image,  $m_{\text{mussels}} = \frac{1}{N_s} \left| \sum_{t=1}^{N_s} x_t \right|$ .

In the next step of the NEATR reconstruction, we use the magnitude estimate  $m_{\text{mussels}}$  as input to a residual CNN (27,28) with U-Net architecture (20). The network aims to learn and mitigate the reconstruction errors in MUSSELS and provide a magnitude image,  $m_{\text{unet}}$ , with minimal artifacts.

## Network Architecture

We used a patch-based U-Net to learn the mapping between the initial reconstruction and its difference to the ground truth magnitude in a slice-by-slice manner. The network consisted of 5 levels (Fig. 2), and the number of convolutional filters was 64 at the highest level. As the size of input was reduced 2-fold by max pooling in the next level, the number of filters was increased 2-fold to retain the total number of kernel weights in each level. The kernels had size 3x3, and each dropout layer set a randomly selected 5% of its input units to zero to help avoid overfitting (29). Leaky ReLU was selected as the nonlinear activation function (30). Batch normalization (BN) was utilized to help accelerate training and avoid saturating nonlinearities (31).

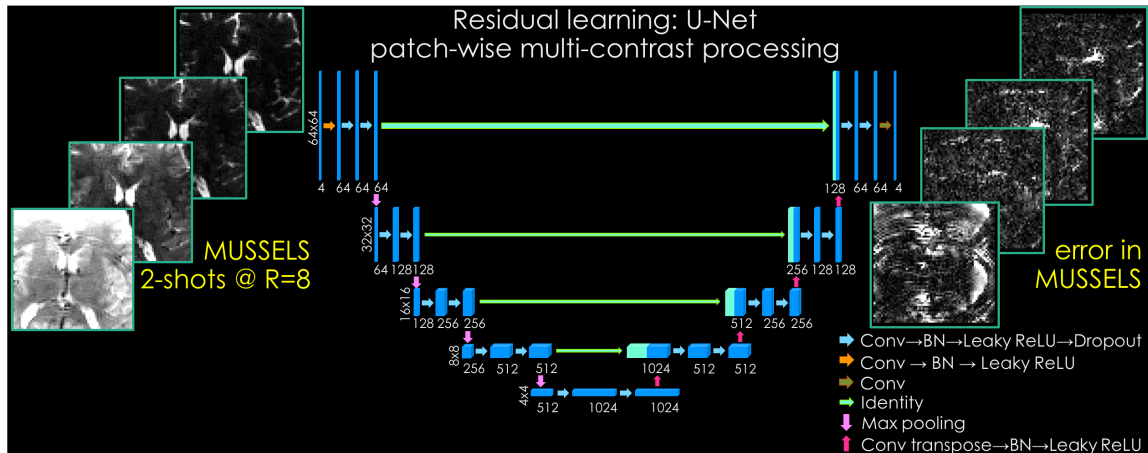


Fig 2. U-Net architecture is used to learn the mapping between patches of multi-echo images reconstructed with MUSSELS, and their difference to reference data. 64x64 patches from 4 echoes are presented as input to a 5-level network, where the first level uses 64 convolutional filters. To help provide scale invariance, max pooling operators downsample the patches after each layer. At the same time, the number of filters are doubled to retain the total number of kernel weights at each level.

## Network Implementation

Keras programming interface (32) with Tensorflow (33) backend were chosen to perform the training. ADAM optimizer (34) was used with learning rate = 0.001 and decay = 0.001. While learning rate acts as a gradient descent step size, decay parameter dampens this step size to take progressively smaller steps in each epoch. An  $\ell_2$  loss function was minimized using 200 epochs and a batch size of 128. An NVIDIA Titan XP graphics card with 12 GB memory was used for training, which took 17 hours.

At the test stage, the patch-based network was applied in a sliding-window manner with a step size of 8 voxels, and the estimated residuals from overlapping patches were averaged together. This process took 4.5 seconds/slice.

## Phase cycling

We keep the improved magnitude image from U-Net  $m_{\text{unet}}$  fixed, and solve only for the image phase of each EPI-shot  $\phi_t$  using phase-regularized parallel imaging, or phase cycling (21):

$$\min_{\phi_t} \|F_t C m_{\text{unet}} \cdot e^{i\phi_t} - d_t\|_2^2 + \alpha \|W \phi_t\|_1 \quad \text{Eq2}$$

Here, only the highlighted phase information  $\phi_t$  is unknown,  $W$  is a wavelet operator that imposes sparsity prior on the shot phase via  $\ell_1$  penalty, and  $\alpha$  is a parameter that controls the degree of regularization. The solution of this problem is made easier by the fact that we are using sensitivity encoding to solve only for the real-valued individual shot phases rather than the complex-valued individual shot images.

## JVC-SENSE

Given estimates of shot-to-shot phase variations  $\phi_t$ , we can now jointly solve for the common magnitude image  $m$  using the data from all shots, through harnessing sensitivity encoding (22) and the virtual coil (VC) concept (16,17) in JVC-SENSE. To do this, we solve a simple least squares problem:

$$\min_m \sum_{t=1}^{N_s} \left\| \begin{bmatrix} F_t C e^{i\phi_t} \\ F_{-t} C^* e^{-i\phi_t} \end{bmatrix} m - \begin{bmatrix} d_t \\ d_{-t}^* \end{bmatrix} \right\|_2^2 + \beta \|m\|_2^2 \quad \text{Eq3}$$

Here, the only unknown is the highlighted magnitude image  $m$ , and the coil sensitivities are modified to include the phase variation in each shot to yield the combined sensitivities  $C e^{i\phi_t}$ . The VC concept is enforced by augmenting the optimization with the conjugate symmetric k-space data  $d_{-t}^*$  and the conjugate sensitivities  $C^* e^{-i\phi_t}$ . Conjugate symmetric k-space is derived from the acquired k-space data by complex-conjugation and flipping the axes in the  $k_x$ - $k_y$  plane. We have used the shorthand notation  $-t$  to express this mirroring operation in k-space. Joint reconstruction across all shots is performed via the

summation operator  $\sum_{t=1}^{N_s}(\cdot)$ . We have chosen to use a simple Tikhonov penalty with the regularization parameter  $\beta$ , but more sophisticated compressed sensing priors could be adopted for further improvement.

## Training Data

In compliance with Institutional Review Board (IRB) requirements, three volunteers were scanned on a Siemens Skyra 3T system with spin-and-gradient-echo (SAGE) (19) msEPI sequence to build a training dataset. Multishot data were collected, where each shot was acquired at R=3-fold acceleration, and a total of 3-shots were acquired with a  $\Delta k_y$  sampling shift between the shots. Relevant parameters were: field of view (FOV) = 220x220x149 mm<sup>3</sup>, matrix size = 142x142x48, echo times (TEs) = 27/73/122/169 ms, repetition time (TR) = 12.6 sec, and echo spacing = 0.313 ms. Each shot sampled 47 phase encoding lines due to R=3-fold acceleration. First two echoes were sampled before the 180° pulse, and the latter two were acquired after the refocusing pulse. Since the acceleration was limited to R=3, we were able to process each shot using GRAPPA (35) (kernel size = 7x7, no regularization) to obtain clean reconstructions. Resulting individual coil images were then combined using coil sensitivity estimates from ESPIRiT (36,37) based on a FLEET calibration acquisition (38). Coil-combined images from the 3-shots were averaged, and an absolute value operation yielded a clean magnitude image which was used as reference. All acquisitions were made with a Siemens 32-channel head coil.

GRAPPA reconstructed data were treated as “fully-sampled” ground-truth, and were *retrospectively* undersampled at rates R=8 and 10 to simulate highly-accelerated msEPI acquisition. Our rationale in acquiring R=3-fold accelerated data rather than an actual R=1 acquisition was to reduce distortion and blurring while still being able to reconstruct high-quality individual shot images to generate the training data.

The retrospectively undersampled msEPI data were then reconstructed using MUSSELS. Due to the very high acceleration rates, the MUSSELS algorithm incurred reconstruction artifacts. These errors with respect to the clean magnitude image were used as the training target in our residual learning approach (**Fig. 2**). Two different networks were trained; one for reconstructions at R=8 and another one for R=10 acceleration.

We extracted 57600 overlapping patches of size 64x64 with a step size of 16 voxels from the training data. The four echoes in the SAGE acquisition were treated as input channels, and were concatenated to create 64x64x4 patches that were fed to the network to enable joint reconstruction across echoes. The training dataset was enriched by 16-fold using augmentations including scaling (0.5x, 1x, 2x), flipping the axes (left-right, anterior-posterior and echo dimension) and rotations ( $\pm 135$ ,  $\pm 90$ ,  $\pm 45$  degrees).



## Reconstruction Experiments and Test Data

**Retrospective acceleration @ R=8 with 2-shots:** msEPI SAGE data were created from datasets acquired at R=3-fold acceleration using 3-shots on a 4<sup>th</sup> subject (not seen during the training of the network.) This acquisition was then reconstructed with GRAPPA to obtain “fully-sampled” k-space data, which served as the “ground-truth” reference to compute root-mean-squared error (RMSE) metrics. Two of the three shots were selected and retrospectively undersampled at an acceleration rate of R=8. The sampling patterns of the two shots were staggered by  $\Delta k=4$  samples to provide complementary k-space coverage.

MUSSELS reconstruction with 100 iterations was performed with window size  $r \times r=3 \times 3$  and  $k=9$  singular values, which was the parameter setting that provided the optimal RMSE. Using Matlab on a workstation with 64 CPU processors and 256 GB memory, our implementation took 63 seconds/slice for reconstruction. MUSSELS magnitude image was then processed with the trained U-Net, which allowed estimation of shot-phases using phase cycling. We used 500 iterations and “db4” wavelets in phase cycling, and set the regularization parameter to  $\alpha=0.01$  for optimal RMSE. Having estimated the phase of each shot, JVC-SENSE with  $\beta=10^{-4}$  was used to compute the final magnitude image. Phase cycling and JVC-SENSE took a total 543 seconds/slice for processing. For all the remaining experiments, we used these reported parameter values without further optimization, except for the  $k$  parameter in MUSSELS during the 3-shot reconstruction as detailed below.

**Retrospective acceleration @ R=10 with 3-shots:** To push the acceleration further, the same test subject’s data were retrospectively undersampled at R=10, and this time all three shots were used in NEATR. The sampling patterns of the shots were staggered by  $\Delta k=\{0, 3, 6\}$  samples to provide complementary k-space coverage and improve joint parallel imaging reconstruction. Since the number of shots was increased, the number of columns in the data matrix  $A$  went up to  $r \times r \times N_s = 3 \times 3 \times 3 = 27$ . In this case, relaxing the number of retained singular values to  $k=11$  provided the optimal RMSE. The remaining parameters were kept the same as changing them did not improve the RMSE performance.

**(Test for generalization #1) Prospective acceleration @ R=8 with 2-shots:** The same test subject was scanned in a different session (using the same scanner) to collect prospectively undersampled msEPI data at R=8-fold acceleration with 2-shots. To keep the contrast similar to the training dataset, TE and TR were kept the same – although a shorter TE/TR combination was possible thanks to the shorter readout period. NEATR was applied using the same parameter setting from the retrospective experiment at R=8.

**(Test for generalization #2) Retrospective acceleration @ R=10 with 3-shots on a different scanner:** Another experiment was performed using msEPI data acquired on a different, 5<sup>th</sup> subject unseen during the training stage. In contrast to all other data acquired on a Skyra system (maximum gradient  $G_{\max} = 40$  mT/m), this last scan was performed using a Siemens Prisma scanner with better gradient hardware performance ( $G_{\max} = 80$  mT/m). The 2-fold increase in  $G_{\max}$  allowed a smaller echo spacing and shorter TEs (19/52/84/117 ms) and TR (9.1 sec), again at R=3-fold acceleration. On average, this led to a 43% reduction in TE and 38% in TR compared to the training protocol. With this last retrospective experiment,

we thus aimed to gauge the effect of contrast differences between the training and test acquisitions. The NEATR parameter setting was kept the same as the earlier R=10 setup.

**Reconstruction *without* ML:** To assess the contribution of the ML step to NEATR, we performed two additional reconstructions *without* U-Net processing. We used the same retrospective undersampling setup from the first two experiments, namely R=8 acceleration with 2-shots and R=10 acceleration with 3-shots. Starting from the MUSSELS magnitude estimate  $m_{\text{musseIs}}$ , we employed phase cycling to solve:

$$\min_{\phi_t} \|F_t C m_{\text{musseIs}} \cdot e^{i\phi_t} - d_t\|_2^2 + \alpha \|W \phi_t\|_1 \quad \text{Eq4}$$

Having obtained refined shot-to-shot phase estimates  $\phi_t$ , we went on to use JVC-SENSE and arrive at a refined magnitude solution. This way, we followed the flowchart outlined in Fig. 1, except that we bypassed the U-Net processing step.

## RESULTS

**Retrospective acceleration @ R=8 with 2-shots (Fig. 3):** For benchmarking, conventional SENSE was applied on each shot *separately* and the reconstructed shot images were complex-averaged to improve SNR. Due to the high acceleration rate, this led to substantial artifacts and large RMSE (28.5%). The rightmost column in Fig. 3 shows the error image averaged over the 4 echoes. Using MUSSELS yielded a large improvement over SENSE with 11.1% error, but residual aliasing and ghosting artifacts were present (yellow arrows). U-Net processing mitigated these aliasing artifacts and improved RMSE to 8.3%, but the network failed to eliminate the signal underestimation that stemmed from the MUSSELS low-rank constraint (white arrows). JVC-SENSE was able to address this underestimation and further improved the image quality with 6.2% error. Supporting Fig. S1 provides a comparison of the shot phase images reconstructed by these techniques for the 2<sup>nd</sup> echo at TE=73 ms, which is the last echo before the refocusing pulse and is expected to contain relatively large shot-to-shot phase differences.

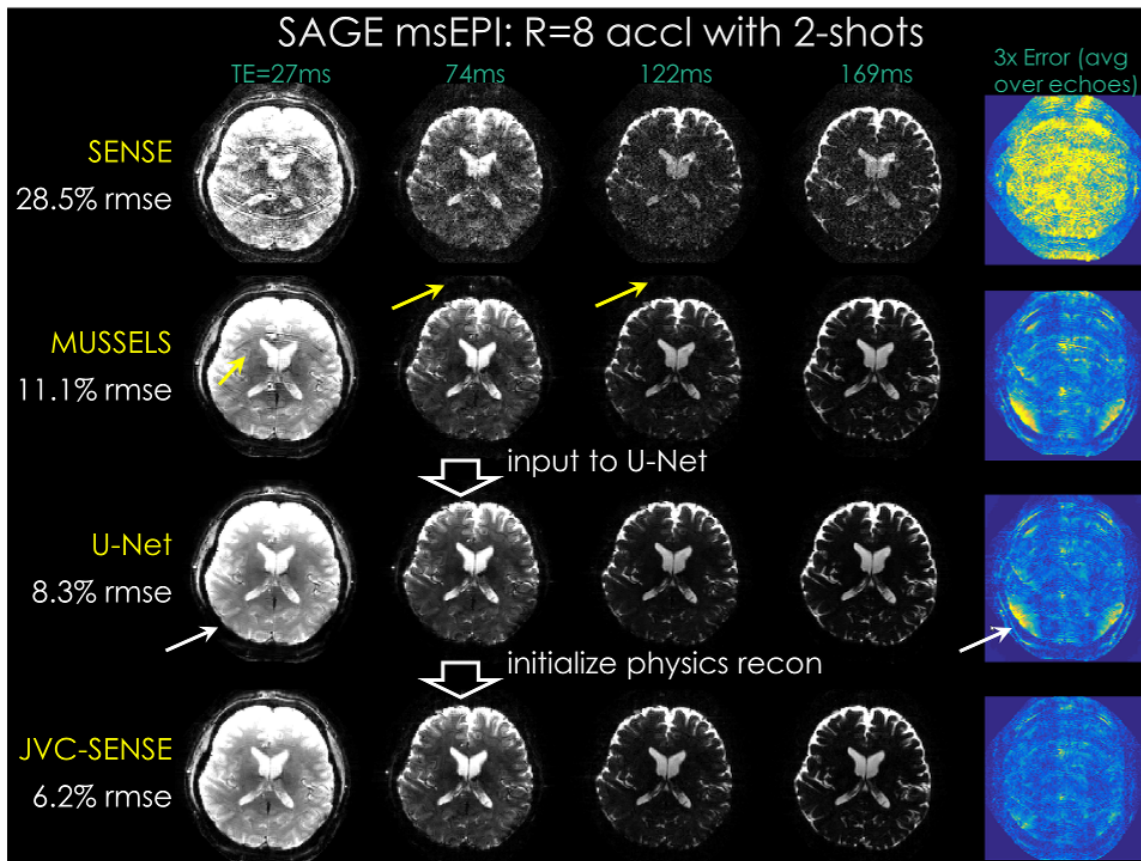
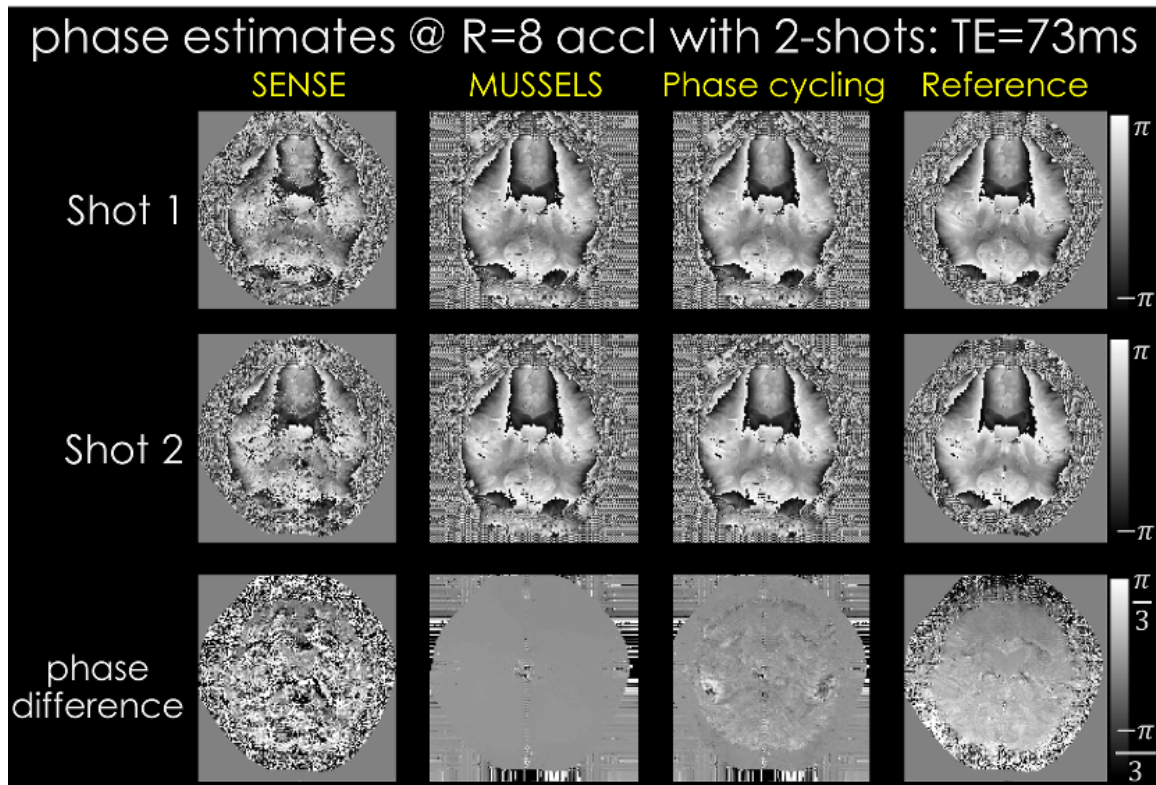


Fig 3. Retrospective R=8-fold acceleration experiment using 2-shots for SAGE msEPI acquisition. Applying a separate SENSE reconstruction per each shot, then averaging the shot-images led to high noise amplification and artifact levels (top row). MUSSELS jointly reconstructed the shot-images to provide marked improvement despite remaining artifacts (yellow arrows, 2nd row). Residual U-Net further cleaned up the MUSSELS solution but some signal underestimation remained (yellow arrows, 3rd row). A final JVC-SENSE reconstruction mitigated these residual errors to provide high-quality images.



Supporting Fig S1. Shot phase estimates of the 2<sup>nd</sup> echo (TE=73 ms) in the SAGE mSEPI experiment using R=8-fold acceleration with 2-shots. First two columns depict the phase of the two individual shot images, whereas the last column shows phase difference between the shots. SENSE phase estimates (1<sup>st</sup> column) are corrupted by noise amplification due to high acceleration, which has been mitigated by MUSSELS thanks to joint reconstruction of the shots (2<sup>nd</sup> column). This however suffered from a structured artifact and was relatively constant in amplitude due to the low-rank constraint. Phase cycling (3<sup>rd</sup> column) failed to eliminate the artifact, but helped capture some of the spatial variation in the phase difference present in the ground truth reconstruction (last column).

**Retrospective acceleration @ R=10 with 3-shots (Fig. 4):** At this high acceleration factor, applying conventional SENSE reconstruction to each shot separately led to substantial artifacts and noise amplification (42.4% RMSE). MUSSELS was much more successful in mitigating these errors, but some residual aliasing and ghosting artifacts are visible (yellow arrows, 11.0% error). Using the MUSSELS solution as input, the U-Net was able to mitigate these artifacts and reduce the RMSE to 6.7%. JVC-SENSE further refined the reconstruction to yield 6.3% error.

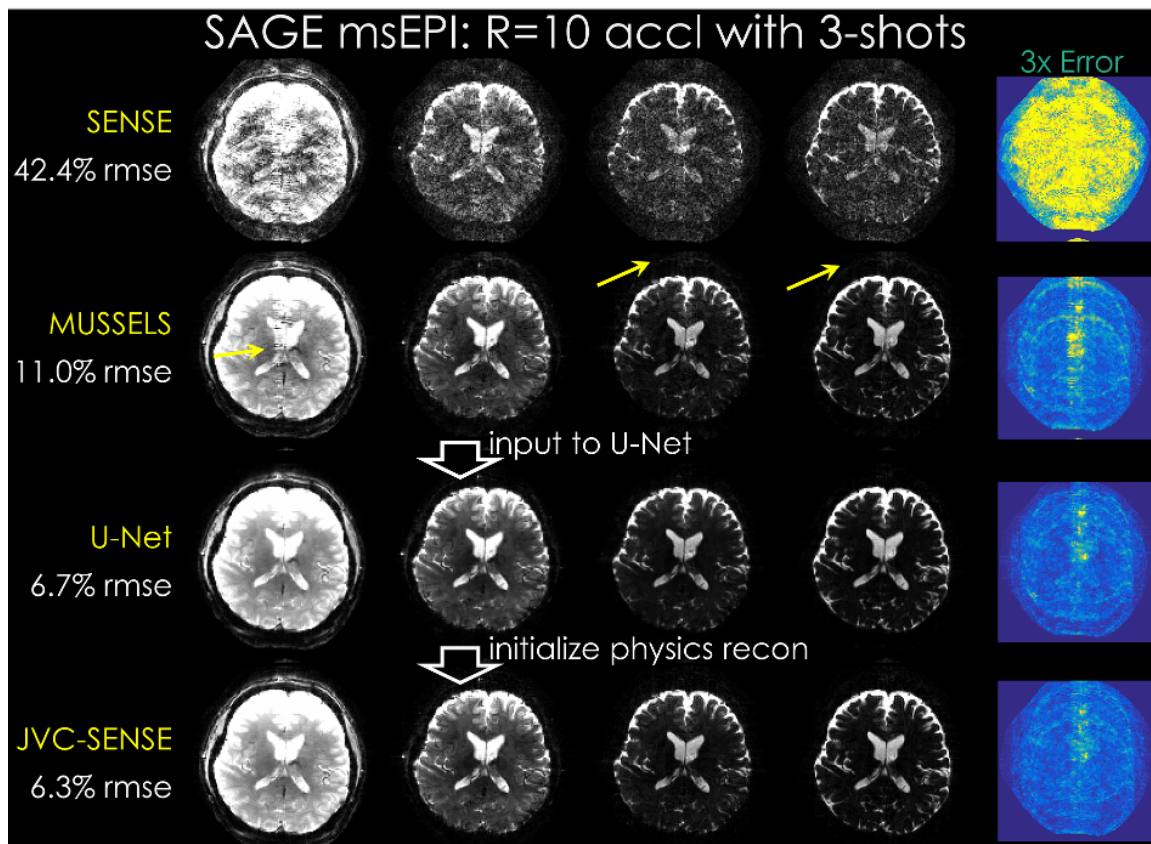


Fig 4. Retrospectively R=10-fold accelerated SAGE msEPI data using 3-shots. Individual SENSE reconstructions per each shot is provided in the first row for benchmarking. MUSSELS provides marked improvement, albeit with residual artifacts (yellow arrows, 2<sup>nd</sup> row). U-Net mitigates these errors (3<sup>rd</sup> row), which are further reduced by JVC-SENSE reconstruction (last row).



(Test for generalization #1) *Prospective acceleration @ R=8 with 2-shots (Fig. 5):* Conventional SENSE reconstruction per shot led to substantial artifacts and noise amplification. MUSSELS provided a large improvement, albeit with some visible aliasing artifacts (yellow arrow). Subsequent U-Net and JVC-SENSE reconstructions were able to largely mitigate, but not fully eliminate this artifact in the first echo.

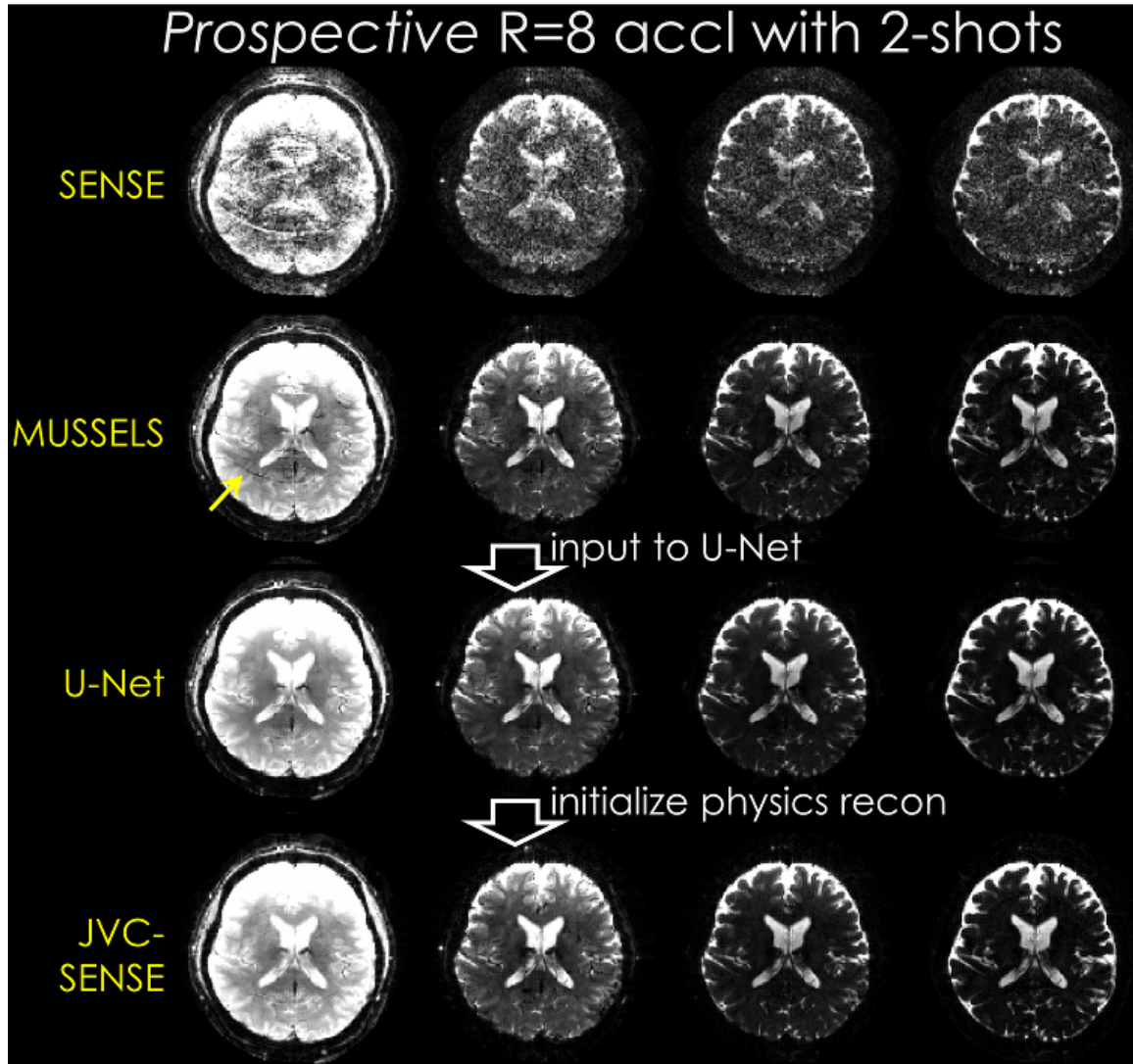


Fig 5. Prospectively undersampled msEPI acquisition at R=8 using 2-shots. Conventional SENSE reconstruction leads to severe artifacts, which are largely mitigated, but not eliminated by MUSSELS (yellow arrow, 2nd row). These errors are further reduced using U-Net and JVC-SENSE, but subtle artifacts were visible in the first echo.

(Test for generalization #2) Retrospective acceleration @ R=10 with 3-shots on a different scanner (Fig. 6): Reconstructing the shots jointly with MUSSELS provided a substantial improvement over an individual SENSE reconstruction per shot, reducing the error from 42.0% to 7.9%. The remaining artifacts that were visible in MUSSELS (yellow arrow) were mitigated using U-Net (6.1% RMSE). A subsequent JVC-SENSE reconstruction yielded the same error metric as the U-Net result (6.1%), with similarly high image quality.

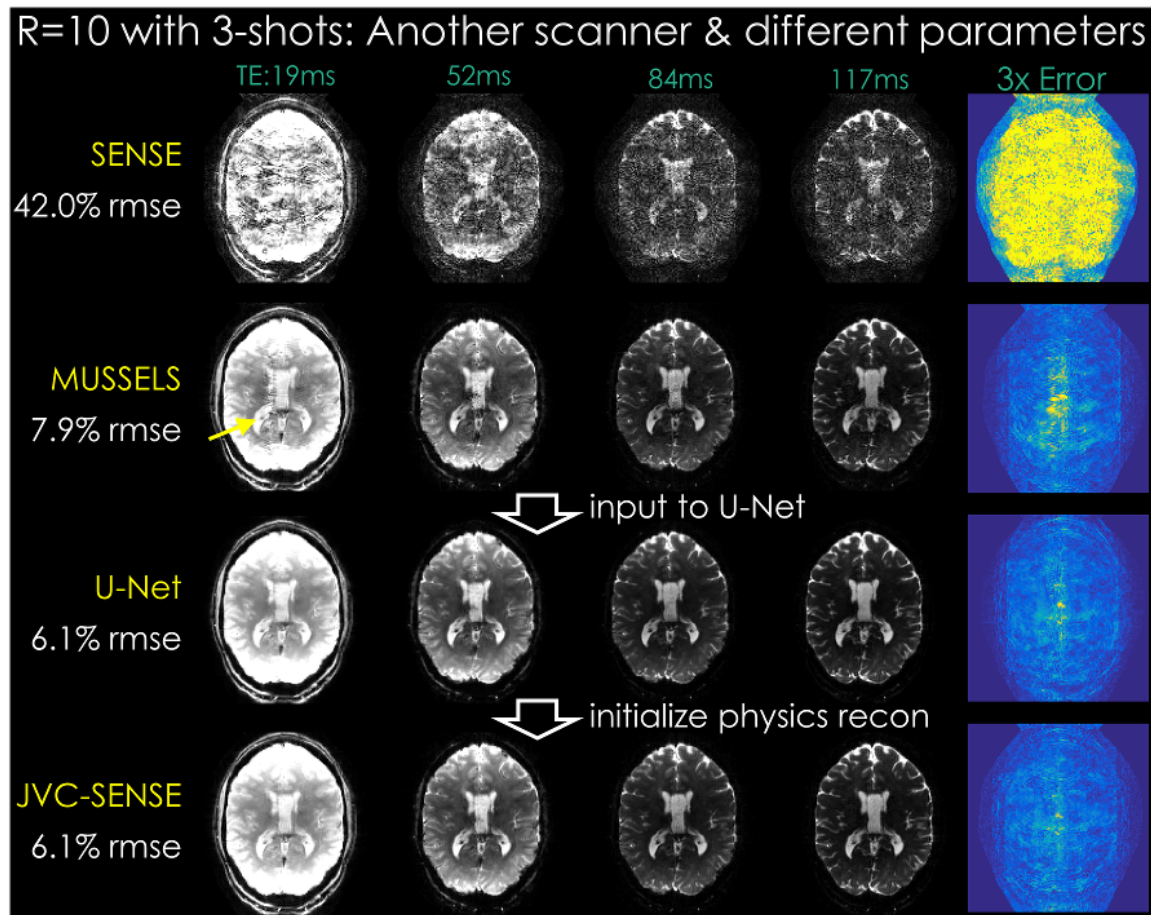


Fig 6. Retrospective undersampling experiment at R=10-fold acceleration using 3-shots. msEPI data were acquired on a different scanner with improved gradient hardware performance to test whether the deep network would generalize despite contrast differences. Separate SENSE reconstructions per each shot are depicted in the first row. MUSSELS yielded much improved images over conventional SENSE, with some artifacts mostly visible on the first echo (yellow arrow, 2<sup>nd</sup> row). U-Net and JVC-SENSE had similar RMSE performance, with similarly high image quality.

**Reconstruction *without* ML (Fig. 7):** At R=8 with 2-shots, phase cycling and JVC-SENSE were able to improve on the initial MUSSELS estimate by reducing the error from 11.1% to 8.3% RMSE. At R=10-fold acceleration using 3-shots, the improvement was relatively small, and these latter physics-based steps reduced the RMSE from 11.0% to 10.0%. In both experiments, artifacts were mitigated, but still visible.

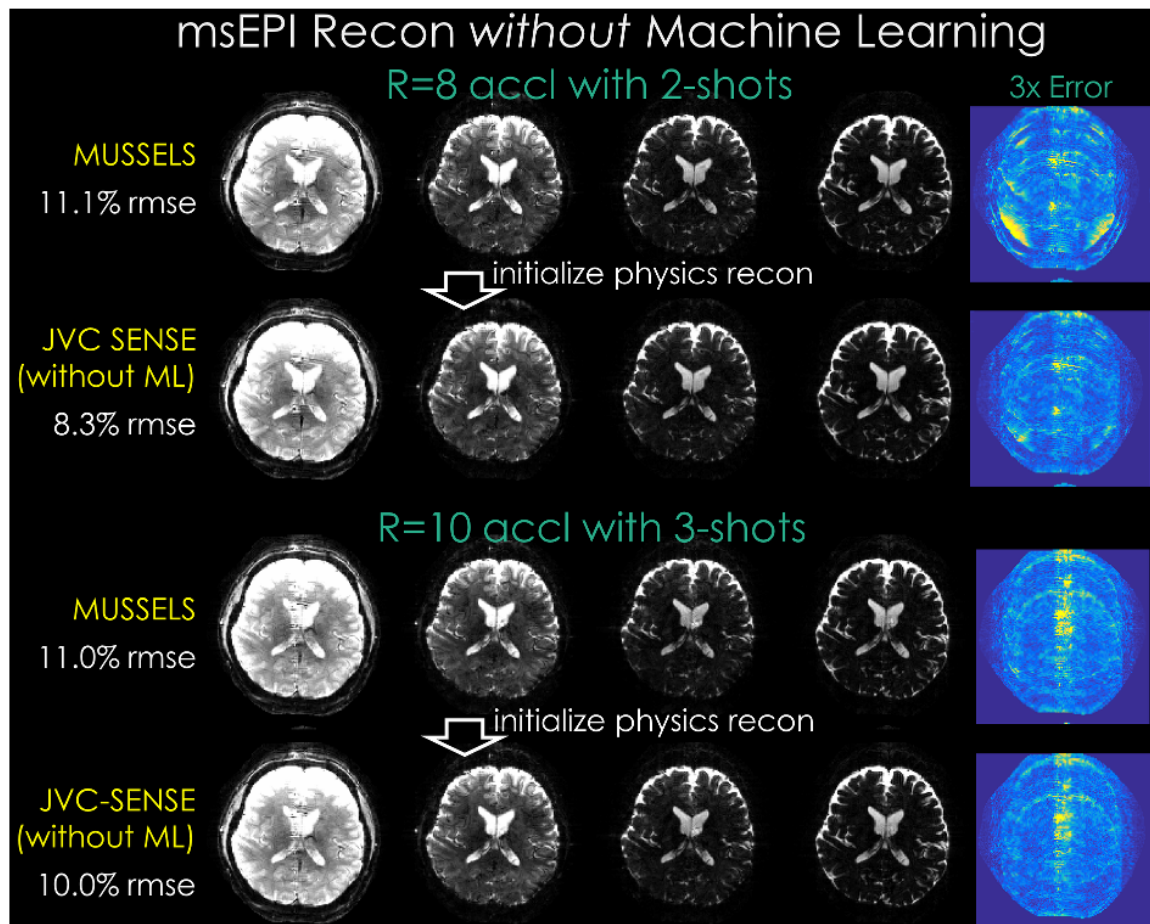


Fig 7. Reconstructions results *without* using machine learning. Starting from the MUSSELS magnitude estimate, subsequent phase cycling and JVC-SENSE steps further refined the reconstruction at R=8-fold acceleration with 2-shots (2<sup>nd</sup> row). Unlike the U-Net aided reconstruction with higher quality and 6.2% RMSE (Fig. 3), reconstruction *without* deep learning incurred 8.3% error. At R=10-fold acceleration using 3-shots, the benefit of the subsequent phase cycling and JVC-SENSE reconstruction was yet smaller, going from 11.0% to 10.0% RMSE with remaining artifacts (last row). On the other hand, using machine learning initialization could reduce the error to 6.3% (Fig. 4) with better artifact mitigation.



## DISCUSSION

We presented NEATR, a synergistic ML and physics-based reconstruction approach, that allowed up to 10-fold accelerated msEPI with high image quality. This was made possible by taking advantage of the state-of-the-art MUSSELS and phase cycling algorithms (11,12,21), Deep Learning, and joint parallel imaging reconstruction. Our residual CNN learned to predict and mitigate the errors in highly accelerated MUSSELS magnitude reconstruction, which then permitted phase cycling to estimate shot-to-shot phase variations. Including this information as additional sensitivity variations then allowed JVC-SENSE to solve for a common magnitude image using the entire multishot k-space data and VC concept.

CNNs can represent very complicated and non-linear input/output relations. While this makes them very powerful, such a complex mapping between input and output causes the network to be difficult to characterize. Since its direct application may lead to unpredictable errors, end-to-end CNN reconstruction in clinical settings is likely to raise acceptance issues. A ML reconstruction approach that can overcome this issue was proposed in the Variational Network (VN) (39) formulation, which allows a transparent deep learning reconstruction of accelerated acquisition where both the kernel weights and nonlinear activation functions are learnt and can be visualized at any layer. VN also utilizes sensitivity encoding and enforces consistency to the acquired k-space data. Similarly, NEATR taps into the potential of CNN without treating it as an end-to-end tool for msEPI, while fully harnessing the encoding provided by the scanner hardware. We achieved this by using CNN to obtain an interim image with minimal artifacts, while utilizing a rigorous physics-based approach to validate and improve upon this solution in the final step of reconstruction. Synergistic combination of ML and physics-based reconstruction proved to be powerful, leading to 70–80% RMSE reduction over our MUSSELS implementation (Figs. 3 and 4). In the absence of Deep Learning initialization, the subsequent phase cycling and JVC-SENSE steps provided a smaller, 10–30% improvement over the MUSSELS reconstruction. The gain was particularly small at R=10-fold acceleration (from 11% to 10% RMSE, Fig. 7) without ML. This was possibly because the acceleration was too high for the phase cycling algorithm to improve on the shot phase estimates without a clean magnitude prior.

Application of msEPI in structural imaging is made difficult by ghosting artifacts from hard-to-estimate physiologic signal changes between shots. Using a standard forward-model based reconstruction would thus necessitate the simultaneous estimation of the image content and the phase variations in each shot. Since both the clean image and the phase information used in the forward-model are unknown, this would entail the solution of a computationally prohibitive, non-convex optimization problem that could get stuck at local minima. As such, existing msEPI techniques circumvent this difficulty by dividing the reconstruction into two separate parts: shot-phase estimation, and combination of multishot given the estimated phase information. Navigator-based approaches derive this phase information from additional calibration acquisitions made for each shot (3–7). MUSE and its extensions (8–10) operate without a navigator, and perform the phase estimation step using parallel imaging to reconstruct a complex image for each shot. Smoothing the phase of each intermediate image then yields an estimate of shot-to-shot physiologic variations, which allows joint reconstruction of all multishot data together.

An exception to this two-step process is MUSSELS (11,12), where a complex image for each shot is reconstructed without explicit shot-phase estimation. This is made possible by exploiting similarities between the shot-images using a low-rank prior on the block-Hankel representation of their k-space. MUSSELS has allowed R=8-fold accelerated msEPI diffusion imaging from as few as 4-shots. Unlike earlier navigator-based (5–7) or navigator-free approaches (8–10) where the number of acquired shots was equal to the acceleration factor ( $N_s=R$ ), MUSSELS could thus perform in the ( $N_s<R$ ) regime to improve acquisition efficiency. With NEATR, we pushed the efficiency gain even further to enable R=8-fold acceleration from 2-shots, and extended the application of msEPI to structural imaging, which has so far been limited to diffusion acquisition. Although MUSSELS had some residual artifacts at such high acceleration, it provided a good initial guess for our residual network to further clean up the magnitude estimate. Starting from this magnitude image, we could then solve for the physiologic variations using phase cycling, which constituted an easier problem since the unknown information was a real-valued phase image. This provided a 2-fold reduction in the number of unknowns compared to a complex-valued SENSE solution.

Rather than refining the magnitude image, an alternative utilization of ML could be to directly estimate the complex-valued shot-images. Although we have not explored this alternative, we think that this could be hampered by two potential issues: (i) Due to physiological noise, phase images are expected to have more variations compared to the magnitude data, which might make it harder for the network to generalize. (ii) Due to the rank constraint, using MUSSELS reconstructed complex shot-images as input to the network may not perform well. For the best RMSE performance at R=8 acceleration with 2-shots, we have found the optimal number of singular values to be  $k=9$ . Given that we are using  $r \times r = 3 \times 3$  windows, this value of  $k$  constrains the reconstruction to be effectively “1-shot” in terms of the degrees of freedom in the data matrix  $A$ . This rank constraint limits the shot-to-shot phase variations that can be represented (Supporting Fig. S1). At R=10-fold acceleration using 3-shots, we have found that relaxing the rank constraint to  $k=11$  provided the best error metric, corresponding to an effective “1.2-shot” ( $=11/9$ ) representation. Further relaxing this constraint could help better capture shot-to-shot differences, at the potential cost of RMSE performance.

**Limitations and their mitigation:** NEATR uses ML to provide an initial estimate to a difficult image reconstruction problem, thereby avoiding the vulnerability of poor generalization of “direct” ML reconstruction. In addition to this, we have augmented our training dataset size by 16-fold to subject the network to greater variation. Using a patch-wise representation with overlapping patches helped further increase the available number of training samples. Finally, we have used a multi-contrast network by inputting magnitude images from multiple echoes in the “channel” axis. This way, residual U-Net could utilize a combination of all input echoes to approximate the MUSSELS error in each individual echo. To test the ability of the network to generalize to an unseen contrast setting, we have acquired data on a different scanner with better gradient hardware performance. Despite the ~40% reduction in the TE/TR parameters due to the shorter echo spacing, U-Net processing did generalize well and mitigated the artifacts in the MUSSELS result (Fig. 6). The subsequent JVC-SENSE reconstruction retained the high image

quality without further improving the RMSE performance. Despite such flexibility in generalization, the network would benefit from retraining if greater differences in sequence parameters, resolution and SNR are dictated by hardware limitations of other scanners.

A more important consideration is the difference in effective echo spacing is between the training data and the highly accelerated test data. We have trained the network on R=3-fold undersampled data so that we could use conventional parallel imaging to reconstruct clean reference images for each shot, while mitigating some of the distortion and blurring artifacts. With this, we aimed to find a good trade-off between the quality of the reference images and their distortion/blurring artifact levels. In the *retrospective* acceleration experiments, the training and test acquisitions were distortion-matched. To check whether the network would generalize to a case where the test data have much less distortion/blurring, we have collected R=8-fold *prospectively* accelerated msEPI data. Although the lack of reference data prevented us from reporting quantitative performance metrics, U-Net processing was able to generalize and provide marked artifact reduction over the MUSSELS reconstruction (Fig. 5). JVC-SENSE performed similarly to U-Net, albeit a subtle artifact could be seen in the first echo image of both reconstructions. A different strategy to ensure that the training and test data have matching echo spacing could be to reduce the readout resolution of the training acquisition. Since parallel imaging artifacts are predominantly along the phase-encoding axis, the loss in readout resolution could have a small impact on learning MUSSELS errors. It could also be possible to start from a distortion-free spin-warp acquisition and simulate msEPI training data using separately acquired B0 maps.

Another consideration is the selection of the reconstruction technique that provides the initial magnitude solution. We have used a POCS-based solver for the MUSSELS formalism, but we note that this differs from the original approach (11) that relied on an Augmented Lagrangian solver (40,41). Other advanced reconstruction strategies such as MUSE (9) or POCS-MUSE (10) could also be utilized to provide this initial estimate.

**Extensions:** We have demonstrated the initial application of NEATR in msEPI SAGE acquisition. Enabling an order of magnitude acceleration in other pulse sequences could help create a multi-contrast msEPI clinical protocol at high in-plane resolution. This would minimize the distortion and blurring artifacts that hamper image quality and achievable resolution in the recently developed singleshot EPI protocols (1,2). Employing msEPI readout in multi-inversion T1 mapping (42,43), FLAIR (44) and diffusion imaging acquisitions with NEATR reconstruction could enable a rapid MR exam with similar table time as a CT scan. Other advanced encoding strategies such as simultaneous multislice (45–50) or wave-EPI (51) could provide additional efficiency gain and/or in-plane acceleration capability.

We believe that the strategy of utilizing ML to estimate unknown nuisance parameters in physics-based forward model reconstructions can be impactful in solving other prohibitively difficult problems. We have recently demonstrated this concept in prospective motion correction (52), where we used residual Deep Learning to provide an interim image with largely reduced motion artifacts. This interim CNN reconstruction provides an initial image and motion parameter estimate thus jumpstarting the physics-

based TAMER algorithm (53), which uses the extra degrees of freedom in multi-coil data to jointly estimate motion parameters and the clean image. Having access to a good initial guess helped the non-convex TAMER optimization converge 30× faster to the final solution. Other venues that might benefit from this synergistic approach could be in navigator-free Nyquist ( $N/2$ ) ghost correction, calibrationless parallel imaging and reference-free k-space trajectory estimation.

## **CONCLUSION**

We demonstrated the ability of NEATR, a combined ML and physics-based reconstruction algorithm, in providing high quality reconstructions from up to 10-fold accelerated msEPI acquisitions using just 2–3 shots of data. The ability to acquire high in-plane resolution images with minimal distortion and blurring could enable an msEPI-based MRI exam with multiple contrasts, while matching the table time of a CT scan.

## **ACKNOWLEDGMENT**

We acknowledge a GPU grant from NVIDIA, and support from NIH NINDS (K23 NS096056) NIMH (R24 MH106096 and R01 MH116173) and NIBIB (U01 EB025162, R01 EB020613, R01 EB019437, R01 EB017337 and P41 EB015896). Additional support was provided by the MGH/HST Athinoula A. Martinos Center for Biomedical Imaging. This research was made possible by the resources provided by NIH Shared Instrumentation Grants S10-RR023401 and S10-RR023043.

## APPENDIX

We pursue a POCS-like solution to the optimization problem posed in the MUSSELS formalism (Eq1), and follow the steps below:

```
Low-rank constraint:
1.  $A = \mathcal{H}(\mathbf{x})$ 
2.  $U\Sigma V^H = \text{svd}(A)$ 
3.  $A = U\Sigma_k V^H$ , where  $\Sigma_k$  is obtained via hard thresholding by keeping the  $k$  largest singular values
4.  $\mathbf{x} = \mathcal{H}^*(A)$ , where  $\mathcal{H}^*$  is a transposed mapping that inserts Hankel matrix elements into multi-shot k-space
5. for  $t = 1:N_s$ 
    $\mathbf{x}_t = \mathbf{x}(:, :, t)$ 
6. Generate coil images by multiplication with sensitivities:
    $\mathbf{x}_c = C\mathbf{x}_t$ 
7. Resubstitute acquired k-space:
    $\mathbf{x}_c = \mathbf{x}_c + F^H(d_t - F_t\mathbf{x}_c)$ 
8. Coil combination:
    $\mathbf{x}_t = (C^H C)^{-1} C^H \mathbf{x}_c$ 
    $\mathbf{x}(:, :, t) = \mathbf{x}_t$ 
end
```

We repeat these steps until convergence, and compute the complex average across the shots and take the absolute value to arrive at the MUSSELS solution,  $m_{\text{mussels}} = \frac{1}{N_s} |\sum_{t=1}^{N_s} \mathbf{x}_t|$ .

## REFERENCES

1. Skare S, Sprenger T, Norbeck O, Rydén H, Blomberg L, Avventi E, Engström M. A 1-minute full brain MR exam using a multicontrast EPI sequence. *Magn. Reson. Med.* 2017;0:1–10. doi: 10.1002/mrm.26974.
2. Nael K, Khan R, Choudhary G, Meshksar A, Villablanca P, Tay J, Drake K, Coull BM, Kidwell CS. Six-minute magnetic resonance imaging protocol for evaluation of acute ischemic stroke: Pushing the boundaries. *Stroke* 2014;45:1985–1991. doi: 10.1161/STROKEAHA.114.005305.
3. Porter DA, Heidemann RM. High resolution diffusion-weighted imaging using readout-segmented echo-planar imaging, parallel imaging and a two-dimensional navigator-based reacquisition. *Magn. Reson. Med.* 2009;62:468–475. doi: 10.1002/mrm.22024.
4. Jeong H-K, Gore JC, Anderson AW. High-resolution human diffusion tensor imaging using 2-D navigated multishot SENSE EPI at 7 T. *Magn. Reson. Med.* 2013;69:793–802. doi: 10.1002/mrm.24320.
5. Liu W, Zhao X, Ma Y, Tang X, Gao J-H. DWI using navigated interleaved multishot EPI with realigned GRAPPA reconstruction. *Magn. Reson. Med.* 2016;75:280–286.
6. Ma X, Zhang Z, Dai E, Guo H. Improved multi-shot diffusion imaging using GRAPPA with a compact kernel. *Neuroimage* 2016;138:88–99. doi: 10.1016/J.NEUROIMAGE.2016.05.079.
7. Dong Z, Wang F, Ma X, Zhang Z, Dai E, Yuan C, Guo H. Interleaved EPI diffusion imaging using SPIRiT-based reconstruction with virtual coil compression. *Magn. Reson. Med.* 2018;79:1525–1531. doi: 10.1002/mrm.26768.
8. Zhang Z, Huang F, Ma X, Xie S, Guo H. Self-feeding MUSE: A robust method for high resolution diffusion imaging using interleaved EPI. *Neuroimage* 2015;105:552–560. doi: 10.1016/J.NEUROIMAGE.2014.10.022.
9. Chen NK, Guidon A, Chang HC, Song AW. A robust multi-shot scan strategy for high-resolution diffusion weighted MRI enabled by multiplexed sensitivity-encoding (MUSE). *Neuroimage* 2013;72:41–47. doi: 10.1016/J.NEUROIMAGE.2013.01.038.
10. Chu M-L, Chang H-C, Chung H-W, Truong T-K, Bashir MR, Chen N. POCS-based reconstruction of multiplexed sensitivity encoded MRI (POCSMUSE): A general algorithm for reducing motion-related artifacts. *Magn. Reson. Med.* 2015;74:1336–1348. doi: 10.1002/mrm.25527.
11. Mani M, Jacob M, Kelley D, Magnotta V. Multi-shot sensitivity-encoded diffusion data recovery using structured low-rank matrix completion (MUSSELS). *Magn. Reson. Med.* 2017;78:494–507. doi: 10.1002/mrm.26382.
12. Mani M, Magnotta V, Kelley D, Jacob M. Comprehensive reconstruction of multi-shot multi-channel diffusion data using mussels. In: 2016 38th Annual International Conference of the IEEE Engineering in Medicine and Biology Society (EMBC). IEEE; 2016. pp. 1107–1110. doi: 10.1109/EMBC.2016.7590897.
13. Liu C, Moseley ME, Bammer R. Simultaneous phase correction and SENSE reconstruction for navigated multi-shot DWI with non-cartesian k-space sampling. *Magn. Reson. Med.* 2005;54:1412–1422. doi: 10.1002/mrm.20706.
14. Pipe JG, Farthing VG, Forbes KP. Multishot diffusion-weighted FSE using PROPELLER MRI. *Magn. Reson. Med.* 2002;47:42–52. doi: 10.1002/mrm.10014.

15. Ong F, Cheng J, Lustig M. Supporting Information for : General Phase Regularized Reconstruction using Phase Cycling. 2017:1–3.
16. Blaimer M, Gutberlet M, Kellman P, Breuer F, Kostler H, Griswold MA. Virtual coil concept for improved parallel MRI employing conjugate symmetric signals. *Magn. Reson. Med.* 2009;61:93–102.
17. Blaimer M, Heim M, Neumann D, Jakob P, Kannengiesser SA, Breuer F. Comparison of phase-constrained parallel MRI approaches: Analogies and differences. *Magn. Reson. Med.* 2016;75:1086–1099.
18. Blaimer M, Jakob P, Breuer F. Regularization method for phase-constrained parallel MRI. *Magn. Reson. Med.* 2014;72.1:166–171.
19. Schmiedeskamp H, Straka M, Newbould RD, Zaharchuk G, Andre JB, Olivot J-M, Moseley ME, Albers GW, Bammer R. Combined spin- and gradient-echo perfusion-weighted imaging. *Magn. Reson. Med.* 2012;68:30–40. doi: 10.1002/mrm.23195.
20. Ronneberger O, Fischer P, Brox T. U-Net: Convolutional Networks for Biomedical Image Segmentation. In: *Medical image computing and computer-assisted intervention : MICCAI*. Springer, Cham; 2015. pp. 234–241. doi: 10.1007/978-3-319-24574-4\_28.
21. Ong F, Cheng JY, Lustig M. General phase regularized reconstruction using phase cycling. *Magn. Reson. Med.* 2018;80:112–125. doi: 10.1002/mrm.27011.
22. Pruessmann KP, Weiger M, Scheidegger MB, Boesiger P. SENSE: Sensitivity encoding for fast MRI. *Magn. Reson. Med.* 1999;42:952–962.
23. Haldar JP. Low-Rank Modeling of Local k-Space Neighborhoods (LORAKS) for Constrained MRI. *IEEE Trans. Med. Imaging* 2014;33:668–681. doi: 10.1109/TMI.2013.2293974.
24. Jin KH, Ye JC. Sparse + Low Rank Decomposition of Annihilating Filter-based Hankel Matrix for Impulse Noise Removal. 2015.
25. Shin PJ, Larson PEZ, Ohliger MA, Elad M, Pauly JM, Vigneron DB, Lustig M. Calibrationless parallel imaging reconstruction based on structured low-rank matrix completion. *Magn. Reson. Med.* 2014;72:959–970. doi: 10.1002/mrm.24997.
26. Samsonov AA, Kholmovski EG, Parker DL, Johnson CR. POCSENSE: POCS-based reconstruction for sensitivity encoded magnetic resonance imaging. *Magn. Reson. Med.* 2004;52:1397–1406. doi: 10.1002/mrm.20285.
27. Zhang K, Zuo W, Chen Y, Meng D, Zhang L. Beyond a Gaussian denoiser: Residual learning of deep CNN for image denoising. *IEEE Trans. Image Process.* 2017;26:3142–3155. doi: 10.1109/TIP.2017.2662206.
28. He K, Zhang X, Ren S, Sun J. Deep Residual Learning for Image Recognition. In: *Proceedings of the IEEE conference on computer vision and pattern recognition.* ; 2016. pp. 770–778.
29. Srivastava N, Hinton G, Krizhevsky A, Sutskever I, Salakhutdinov R. Dropout: A Simple Way to Prevent Neural Networks from Overfitting. *J. Mach. Learn. Res.* 2014;15:1929–1958.
30. Maas AL, Hannun AY, Ng AY. Rectifier nonlinearities improve neural network acoustic models. *ICML Work. Deep Learn. AUDIO, SPEECH Lang. Process.* 2013;30:3.
31. Ioffe S, Szegedy C. Batch normalization: Accelerating deep network training by reducing internal

- covariate shift. *Int. Conf. Mach. Learn.* 2015:448–456.
32. Chollet F. <https://keras.io>. 2015.
33. Abadi M, Agarwal A, Barham P, et al. TensorFlow: Large-Scale Machine Learning on Heterogeneous Distributed Systems. 2016.
34. Kingma D, Ba J. Adam: A method for stochastic optimization. *arXiv Prepr.* 2014:arXiv:1412.6980.
35. Griswold MA, Jakob PM, Heidemann RM, Nittka M, Jellus V, Wang J, Kiefer B, Haase A. Generalized autocalibrating partially parallel acquisitions (GRAPPA). *Magn. Reson. Med.* 2002;47:1202–1210. doi: 10.1002/mrm.10171.
36. Uecker M, Lai P, Murphy MJ, Virtue P, Elad M, Pauly JM, Vasanawala SS, Lustig M. ESPIRiT-an eigenvalue approach to autocalibrating parallel MRI: Where SENSE meets GRAPPA. *Magn. Reson. Med.* 2014;71:990–1001. doi: 10.1002/mrm.24751.
37. Uecker M, Ong F, Tamir JI, Bahri D, Virtue P, Cheng JY, Zhang T, Lustig M. Berkeley Advanced Reconstruction Toolbox. In: *Proceedings of the International Society for Magnetic Resonance in Medicine.* ; 2015. p. 2486.
38. Polimeni JR, Bhat H, Witzel T, Benner T, Feiweier T, Inati SJ, Renvall V, Heberlein K, Wald LL. Reducing sensitivity losses due to respiration and motion in accelerated echo planar imaging by reordering the autocalibration data acquisition. *Magn. Reson. Med.* 2016;75:665–679. doi: 10.1002/mrm.25628.
39. Hammernik K, Klatzer T, Kobler E, Recht MP, Sodickson DK, Pock T, Knoll F. Learning a variational network for reconstruction of accelerated MRI data. *Magn. Reson. Med.* 2018;79:3055–3071. doi: 10.1002/mrm.26977.
40. Goldstein T, Osher S. The Split Bregman Method for L1-Regularized Problems. *SIAM J. Imaging Sci.* 2009;2:323–343. doi: 10.1137/080725891.
41. Ramani S, Fessler JA. Parallel MR Image Reconstruction Using Augmented Lagrangian Methods. *IEEE Trans. Med. Imaging* 2011;30:694–706. doi: 10.1109/TMI.2010.2093536.
42. Renvall V, Witzel T, Wald LL, Polimeni JR. Automatic cortical surface reconstruction of high-resolution T1 echo planar imaging data. *Neuroimage* 2016;134:338–354. doi: 10.1016/J.NEUROIMAGE.2016.04.004.
43. Cohen O, Polimeni JR. Optimized inversion-time schedules for quantitative T1 measurements based on high-resolution multi-inversion EPI. *Magn. Reson. Med.* 2017. doi: 10.1002/mrm.26889.
44. De Coene B, Hajnal J V., Gatehouse P, Longmore D, White SJ, Oatridge A, Pennock JM, Young Ian R, Bydder GM. MR of the Brain Using Fluid-Attenuated Inversion Recovery (FLAIR) Pulse Sequences. *Am. J. Neuroradiol.* 1992;13:1555–1564.
45. Feinberg DA, Moeller S, Smith SM, Auerbach E, Ramanna S, Glasser MF, Miller KL, Ugurbil K, Yacoub E. Multiplexed Echo Planar Imaging for Sub-Second Whole Brain fMRI and Fast Diffusion Imaging Valdes-Sosa PA, editor. *PLoS One* 2010;5:e15710. doi: 10.1371/journal.pone.0015710.
46. Setsompop K, Gagoski BA, Polimeni JR, Witzel T, Wedeen VJ, Wald LL. Blipped-controlled aliasing in parallel imaging for simultaneous multislice echo planar imaging with reduced g-factor penalty. *Magn. Reson. Med.* 2012;67:1210–1224. doi: 10.1002/mrm.23097.



47. Larkman D, Hajnal J, Herlihy A. Use of multicoil arrays for separation of signal from multiple slices simultaneously excited. *J. Magn. Reson. Imaging* 2001;13:313–317.
48. Weaver JB. Simultaneous multislice acquisition of MR images. *Magn. Reson. Med.* 1988;8:275–284. doi: 10.1002/mrm.1910080305.
49. Uğurbil K, Xu J, Auerbach EJ, et al. Pushing spatial and temporal resolution for functional and diffusion MRI in the Human Connectome Project. *Neuroimage* 2013;80:80–104. doi: 10.1016/j.neuroimage.2013.05.012.
50. Moeller S, Yacoub E, Olman CA, Auerbach E, Strupp J, Harel N, Uğurbil K. Multiband multislice GE-EPI at 7 tesla, with 16-fold acceleration using partial parallel imaging with application to high spatial and temporal whole-brain fMRI. *Magn. Reson. Med.* 2010;63:1144–1153. doi: 10.1002/mrm.22361.
51. Poser BA, Bilgic B, Gagoski BA, Uludag K, Stenger VA, Wald LL, Setsompop K. Echo-planar imaging with wave-CAIPI acquisition and reconstruction. In: International Society for Magnetic Resonance in Medicine 25th Scientific Meeting, Hawaii. ; 2017. p. 1198.
52. Bilgic B, Cauley SF, Chatnuntawech I, Manhard MK, Wang F, Haskell M, Liao C, Wald LL, Setsompop K. Combining MR Physics and Machine Learning to Tackle Intractable Problems. In: Proceedings of the 26th Annual Meeting ISMRM. ; 2018.
53. Haskell MW, Cauley SF, Wald LL. Targeted Motion Estimation and Reduction (TAMER): Data Consistency Based Motion Mitigation for MRI using a Reduced Model Joint Optimization. *IEEE Trans. Med. Imaging* 2018:1–1. doi: 10.1109/TMI.2018.2791482.